AppliedMath

MDPI

Article

Agent-Based Simulation of the Infection Risk in Variable Indoor Geometries

Mathias Wagner [1], Thomas Harweg [2], Roland Linder [3] and Frank Weichert [2,*]

[1] Department of Pathology, Medical School, University of Saarland, 66421 Homburg, Germany; mathias.wagner@uks.eu
[2] Department of Computer Science VII, Technical University Dortmund, 44227 Dortmund, Germany; thomas.harweg@tu-dortmund.de
[3] Institute of Medical Informatics, University of Luebeck, 23538 Luebeck, Germany; roland.linder@uni-luebeck.de
* Correspondence: frank.weichert@tu-dortmund.de; Tel.: +49-231-755-6122

Abstract

In this paper, we introduce an agent-based pedestrian simulation with aerosol modeling, which we use for analyzing the risk of infection with airborne diseases, with special attention to indoor scenarios and the corresponding geometry. For our analysis, we simulate a realistic supermarket scenario, and analyze the influence of geometric factors for the risk of infection regarding aerosol concentration. Using such a defined set of geometry allows for a targeted analysis of risk factors. Specifically, we examine if angular structures bear higher viral loads than flat structures, which is confirmed by our experiments. An artificial neural network (ANN) specifically trained on simulation data is able to identify adjacent geometric structures based on aerosol concentration with up to 94% accuracy.

Keywords: pedestrian simulation; agent-based model; aerosol modeling; infectious diseases; indoor scenarios

1. Introduction

At the end of 2019, a novel coronavirus disease (COVID-19) was first identified in Wuhan, China [1]. Within a few months, the infection spread rapidly across the globe, resulting in an unprecedented pandemic and causing over 431,000 deaths during the initial wave [2]. The disease is attributed to Severe Acute Respiratory Syndrome Coronavirus 2 (SARS-CoV-2). Despite extensive public health interventions and restrictions on daily life, the number of new infections continued to increase worldwide [3]. In general, the transmission of infectious pathogens through the air is a key problem in infection epidemiology. Various other airborne respiratory pathogens are responsible for infections, e.g., influenza viruses, rhinoviruses, respiratory syncytial virus (RSV), and adenoviruses [4,5]. In principle, bacteria and fungi must also be taken into account [6].

The characterization "airborne respiratory pathogen" is a rather imprecise generic name coined to address diverse entities that differ in seasonality of circulation, modes of spread, transmissibility, susceptible populations, and the severity of symptoms. Airborne viruses, a subset of airborne respiratory pathogens, may be transmitted by direct (physical) and/or indirect (fomite-mediated) contact and by droplets and/or aerosols (with a debatable particle size threshold between "large" droplets and "fine" aerosols) [7]. Despite numerous precautionary measures, aeration and ventilation appear to be crucial

Academic Editor: Wei Yao

Received: 12 March 2026
Revised: 17 May 2026
Accepted: 21 May 2026
Published: 31 May 2026

from the viewpoint of exposure reduction to airborne viruses in enclosed spaces as virus-contaminated aerosols still pose a serious problem indoors. The present study therefore focuses on room dividers that can be applied to segment large rooms into smaller "pseudo-insulated" sections and their possible effect on the spread of airborne viruses. Despite the fact most self-serve supermarkets around the globe tend to inveigle their customers into spending as much time as possible within their doors, shopkeepers have introduced a variety of changes to minimize the risk of infection with airborne respiratory pathogens while shopping [8].

Analyses using intelligent, agent-based models are available to investigate the risk of airborne transmission of a virus in supermarkets [9,10]. These analyses also consider the risk of infection associated with random movement and interaction patterns of people in public indoor spaces in combination with the aerosol dispersion equation and pedestrian agent models. It is, however, still unclear whether, in light of possible virus spread, a distinction is to be made between straight aisles and aisles with corners. This may be tested in an abstract environment with a parallel versus a perpendicular orientation of shelves (synonym: dividers). Perpendicularity would then be defined as shelves set up to form concave corners with an inner angle of 90° [11] as opposed to Euclidean parallelism in which the dividers are placed along straight lines (i.e., "normal edges" [12]) that lie in a common plane and do not intersect in three-dimensional space. The task would be to assess the relative risk of infection at concave corners compared to what are considered "cornerless points" [13].

The objective of this paper is to investigate the potential for integrating established concepts for modeling variable geometries into an agent-based simulation framework for the study of infectious events. The objective of this study is twofold: firstly, to examine the efficacy of mathematical models and associated investigations in enhancing comprehension of the significance of geometric characteristics, and secondly, to explore the potential of these models and investigations to inform future geometric analysis. In this study, the modeling of a supermarket using the geometric elements of the game TETRIS [14] was examined as an example. The geometric elements, which are more commonly referred to as "tetrominoes" (synonyms: "blocks", "pieces", "units", and "zoids"), comprise seven different rotatable two-dimensional one-sided geometric shapes. Each of these shapes consists of four equal-sized squares (synonym: "cell") which are connected at their edges, and not just at their corners (see Figure 1). The geometric elements under consideration are employed for the purpose of modeling a supermarket, with a particular focus on the shelves. The simulation introduced here was designed to take place in a virtual representation of a standard shop with aisles, walls, shelves, and sale and cash desks, as previously described elseplace [15].

On the resulting simulation data, we use an artificial neural network approach in order to analyze how well geometric properties can be predicted from associated numerical values.

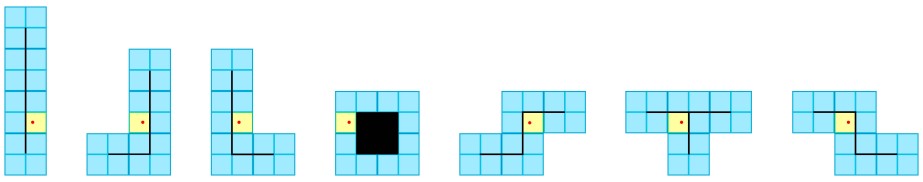

Figure 1. The seven basic tetromino shapes used (I, J, L, O, S, T, Z), divided into subblocks (blue), with geometry (black), waypoints (red), and the containing subblock marked yellow.

2. Related Work

Mathematical models and simulations designed to predict the behavior of SARS-CoV-2 and the outcome of COVID-19 may be viewed as a dime a dozen [16–18]. One of the modeling techniques in the context of coronavirus infection uses a collection of autonomous entities referred to as "agents", who individually assess their situation to make decisions on the basis of a set of rules [19,20]. As indoor environments are a significant venue for the transmission of SARS-CoV-2 [21], various agent-based models have been implemented to evaluate the risk of SARS-CoV-2 transmission in publicly accessible indoor facilities such as supermarkets [22,23] or typical lecture halls [24]. Other studies, such as [25], use a stochastic model to examine the transmission dynamics of hepatitis B and highlight the importance of vaccination and control measures in containing the disease.

There are numerous comprehensive reviews on research into the simulation of pedestrian movements [26,27]. The models are predominantly divided into macroscopic and microscopic approaches. Macroscopic models consider the crowd as the smallest unit, while microscopic models consider individual pedestrians—this allows for a more realistic description of the behavior of individual persons. While the authors of the present study have previously presented an approach which describes agents emulating fully susceptible people in a supermarket under the threat of a single lineage of SARS-CoV-2 [15], the currently introduced setting is inert to the number of virus lineages, the percentage of possibly non-vaccinated individuals, or the effects of a vaccine breakthrough on infection statistics as it focusses on a possible risk associated with a particular architectural feature.

Based on the ancient connection between architecture and geometry [28], the use of well-defined geometric figures such as Tetris-style tetrominoes was deemed advantageous when testing the hypothesis that geometric forms in architecture might play a role in the indoors spread of SARS-CoV-2. Although there has been considerable research into the mathematics behind the game of TETRIS and its game pieces [29–31], and aspects of the game have been used across a diverse range of applications, including neuroscience [32,33], sensor technology [34], and architecture [35], the current study seems to be the first to apply the tetrominoes of TETRIS to systematically describe details of the spread of SARS-CoV-2 in a shop with an entrance, cashiers and an exit, as well as aisles surrounded by shelves.

As it is still unclear whether architectural concave vertexes with an inner angle of 90° [11] are contributing to a higher risk of infection with SARS-CoV-2 than geometries referred to as "normal edge" [12], an agent-based model was implemented to simulate the indoor traffic of unrelated people in a room full of obstacles.

3. Materials and Methods

In the following, we describe our agent-based simulation, including the mathematical definitions of pedestrian dynamics, infectious disease modeling, and the modeling of the geometry, which incorporates the embedding of TETRIS building blocks. The simulation described here is based on a custom software implementation specifically tailored to this study.

3.1. Pedestrian Dynamics

The simulation is based on a social-force model for pedestrian dynamics [36]. Each pedestrian is modelled by an agent $p_i = \left(\mathbf{x}_i, \mathbf{v}_i, \mathbf{e}_i^0, v_i^0, \mathbf{s}_i, \mathbf{d}_i, c_i, c_i^{\text{aexp}}\right)$. The associated variables and attributes will be explained in the following.

Agent movement is determined by the equation of motion

$$\frac{\mathrm{d}\mathbf{v}_i}{\mathrm{d}t} = \mathbf{f}_i^0 + \mathbf{f}_i^{\text{wl}} + \mathbf{f}_{ij}, \tag{1}$$

where $\mathbf{v}_i$ denotes the current velocity of agent p_i, and $\mathbf{f}_i^0$, $\mathbf{f}_i^{\mathrm{wl}}$, and $\mathbf{f}_{ij}$ denote self-acceleration, wall, and agent–agent forces, respectively. The force $\mathbf{f}_i^0$ for self-acceleration is given by

$$\mathbf{f}_i^0 = \frac{\mathbf{v}_i^0 \mathbf{e}_i^0 - \mathbf{v}_i(t)}{\tau} \tag{2}$$

where v_i^0 is the desired speed (m/s) of p_i, $\mathbf{e}_i^0$ is its desired direction, and τ is a relaxation constant, measured in seconds. Note that, as in the original model [36], a term for mass is not provided. The wall force $\mathbf{f}_i^{wl}(d_\mathbf{w})$ determines the interaction of an agent with an obstacle $\mathbf{w} \in \mathbb{R}^2$, with $\mathbf{w}$ denoting the position of the obstacle (or part of the obstacle). It is calculated as

$$\mathbf{f}_i^{\mathrm{wl}}(d_\mathbf{w}) = a \exp\left(\frac{-d_\mathbf{w}}{b}\right)\mathbf{n}_\mathbf{w}. \tag{3}$$

Here, $d_\mathbf{w}$ is the distance of p_i from the (closest) obstacle $\mathbf{w}$, a and b are model constants, and $\mathbf{n}_\mathbf{w}$ denotes the normal from $\mathbf{w}$ to p_i. Interaction between two agents, p_i and p_j, is determined by agent–agent forces $\mathbf{f}_{ij}$:

$$\mathbf{f}_{ij}(d,\theta) = -\hat{a}\exp\left(\frac{-d}{\hat{b}}\right)\left[\exp\left(-\left(n'\hat{b}\theta\right)^2\right)\mathbf{t}_{ij} + \hat{k}\exp\left(-\left(n\hat{b}\theta\right)^2\right)\mathbf{n}_{ij}\right]. \tag{4}$$

With d being the distance between two agents p_i and p_j, and $\hat{b} = \gamma\|\mathbf{t}'\|$, $\hat{k} = \operatorname{sgn}\theta$, and $\hat{a}, n, n'$ being the model parameters. The vector $\mathbf{t}_{ij}$ denotes the so-called "interaction direction" between p_i and p_j, calculated by normalizing $\mathbf{t}' = \lambda(\mathbf{v}_i - \mathbf{v}_j) + \mathbf{e}_{ij}$ to length 1, and $\mathbf{n}_{ij}$ denotes the vector normal to $\mathbf{t}_{ij}$, oriented to the left. Finally, θ is the angle between $\mathbf{t}_{ij}$ and $\mathbf{e}_{ij}$, with the latter being the normalized direction pointing from p_i to p_j. This force is calculated for all pairs (i, j) of agents and summed up for each agent. The constant model parameters are listed in Table 1, which also includes the corresponding identifiers used in the original publication, if differing.

Table 1. Model parameter values [36].

Parameter	Value
$\hat{a}$ (A in [36])	4.5 ± 0.3
n	2.0 ± 0.1
n'	3.0 ± 0.7
γ	0.35 ± 0.01
λ	2.0 ± 0.2
τ	0.54 ± 0.05 s

3.2. Simulation Domain Modeling and Pathfinding

The simulation is carried out on a rectangular area $\Omega \subset \mathbb{R}^2$, which represents an actual two-dimensional environment of size $w \times h$ in meters. On this area, a floor plan given by a two-dimensional binary map F defines the walkable space and obstacles. The size $w_F \times h_F$ of the floor plan F is given in pixels (px), with a resolution factor $s_F = w_F/w = h_F/h$ determining the ratio of pixels per meter. There are no considerable limitations as to the composition of the floor plan, making our simulation suitable for many real-world scenarios, well beyond the one presented here. For the efficient determination of the distance d_w between agents and obstacles, we use the distance transform [37,38]. Within the walkable area of F, we define starting, way, and destination points. These points are denoted by s_k, w_k, and d_k and subsumed in sets S, D_W, and D_D, respectively. The agents' pathfinding is brought about by using Dijkstra's algorithm [39]. To this end, a direction map $\mathbf{D}_k^{\mathrm{dir}} \in \mathbb{R}^{h_F \times w_F}$ is created for every destination point $\mathbf{d}_k \in D = D_D \cup D_W$. For every

grid point $\mathbf{x} \in \{0, \ldots, h_F - 1\} \times \{0, \ldots, w_F - 1\}$ within F, this map contains the direction along the shortest path towards the corresponding destination point.

3.3. Pedestrian Simulation

The simulation operates on a set of agents P_{sim} of fixed size $n = |P_{\text{sim}}|$ which are active at the same time. This set of agents is drawn from a global agent pool P_{pool} of a larger size, i.e., $|P_{\text{pool}}| \gg |P_{\text{sim}}|$. The simulation runs over a defined period of time $t_{\text{total}} = [t_0, t_{\max}]$, measured in seconds. At the beginning of the simulation (timestep t_0), agents are placed randomly at walkable positions according to a uniform distribution with regard to the (rectangular) area. An agent's initial starting point is thus referred to as $\mathbf{s}_i(t_0) = \mathbf{x}_i(t_0)$. During the simulation, agents move towards their current individual destination point $\mathbf{d}_i(t)$, which can be either a way point or final destination point. If an agent has reached a way point, it gets assigned a new destination point, which can again be from either category. If an agent has reached a final destination point, it is removed from the simulation and a new agent from the global pool P_{pool} is added to the running simulation at one of the available starting points, which is again randomly chosen from a uniform distribution. Generally, the size of the population as well as the number and placement of the points of interest can be arbitrarily chosen, contributing to the adaptability of our simulation to different and realistic scenarios.

3.4. Infectious Disease Modeling

We model infectious disease transmission by keeping track of aerosol virus concentration over space and time. We do so by employing a rather simple model based on tracking agent trajectories and approximated aerosol diffusion, and more complex phenomena of fluid dynamics, such as convection or turbulence, are not taken into consideration. Furthermore, our model is strictly two-dimensional and does not take into account any height- or gravity-related effects. To model virus concentration within the simulated area Ω, we create a two-dimensional aerosol map, $\phi^{\text{ae}} \in \mathbb{R}^{h_F \times w_F}$, of the same size (and resolution), $w_F \times h_F$, as the binary floor map F, storing the virus concentration at each position. This concentration is initially zero everywhere and increases as infectious agents move over the map. This calculation is done for equally sized time windows of length t_{frame}, measured in seconds, over the whole duration of the simulation. For each position $\mathbf{x}_i$ of the agent's trajectory within the time window, a certain amount c^{ae} (measured in RNA/cm^3) is distributed over a disk area of radius r_{ae}, and added to the map ϕ_j^{ae} cumulatively, with j being the index to the respective time window.

Aerosol diffusion is approximated by a Gaussian blur filter, which is applied after each step. To prevent the diffusion process from permeating through walls, the map ϕ^{ae} is set to zero at all positions containing obstacles at the end of each step. To finally determine an (non-infected) agent's p_i exposure to contaminated aerosol, the values of ϕ_j^{ae} along the agent's own trajectory are summed up, resulting in c_i^{aexp}. To further evaluate the agents' movements and their distribution, we also calculate heatmaps $\phi_j^{\text{ht}} \in \mathbb{R}^{h_F \times w_F}$ for each time frame. This map stores information about the cumulated time of stay of agents for each position of the simulated area. It is calculated as the two-dimensional histogram of the agent trajectories, with each discrete grid cell of the map considered a histogram bin.

3.5. Geometry Modeling

The floor plan of an actual supermarket serves as a basis for the simulation area. It consists of an entry area, a main area, and an exit area. We populate the main area with geometry based on the game TETRIS (cf. Figure 1), which is varied according to geometric properties of the blocks for the different experiments performed. The total (rectangular) size

of the floor map is 2497 × 1081 px ($W \times H$), which equals an actual size of 72.6 × 31.4 m^2, at a resolution of $s_F = 34.4\,\text{px/m}$. The floor plan is based on data of a standard German supermarket (size and basic layout), which is similar to the one examined elsewhere [40]. Based on this plan, we created a layout tailored specifically to the experiments performed, as described in Section 4. As mentioned above, we divide the floor plan into three areas: the entrance area, the area containing cashiers and exits, and the main area (cf. Figure 2). Within the entrance and exit areas, we define fixed starting, way, and destination points, which do not change for all simulations. The sizes of the entrance and cashier areas are 27.7 m × 16.6 m and 27.7 m × 12.8 m, respectively.

The main area holding the TETRIS geometry is divided into a rectangular grid of size 33 × 20 ($W \times H$) (the inner area is of size 1697 × 1041 px, or 49.3 m × 30.3 m), with the cell size corresponding exactly to the size of a tetromino subblock. Due to the margins at the borders, a grid area of 31 × 18 is effectively used. The actual configurations for the geometry and the process of creating them will be described in the following, as well as in Section 4.

For the creation of the inner geometry of the main area, we draw on seven types of TETRIS building blocks ("tetrominoes", I, J, L, O, S, T, and Z), as shown in Figure 1. For each tetromino, four variants are derived, one basic shape and three more, resulting from rotations by 90°, 180°, and 270° (cf. Figure 3). All individual tetrominoes are built from different arrangements of exactly four square blocks, and each of these blocks is further subdivided into four subblocks (Figure 1). A tetromino thus consists of 16 subblocks. The size of a subblock is 52 px, which equals an actual size of 1.51 m. The size was chosen to be in accordance with the interior geometry of the original floor plan. The actual geometry used in the simulation is equal to the inner "skeleton" of the tetrominoes, i.e., the area with (Manhattan) distance of one subblock side-length to the outer boundary. Each tetromino has a defined subblock which contains one fixed way point. The subblocks are numbered uniquely over all tetrominoes, ordered by orientation and type. The resulting three-digit numbers XYZ can thus be used to identify tetromino type and orientation, later. The subblocks containing a waypoint (marked yellow in Figure 1) receive special attention. Numbering starts there and is counted up by tetromino type (within the group with the same orientation). In other words, the subblock of the I-Tetromino with 0° orientation containing a point of interest (POI) is 001, for J 002, for L 003, and up to Z 007. From there on, the identifying numbers are simply counted up, starting again at the next I-Tetromino subblock and increasing first over the same tetromino (clockwise), then with the other tetromino types in the same orientation, ending at 112 with the "last" subblock of Tetromino Z. For the next batch of tetromino orientation, X is counted up by one, resulting in 201 for the POI of Tetromino I with orientation 90°. X thus indicates orientation, and $X \in \{0,1\}$ equals 0°, $\{2,3\}$ 90°, $\{4,5\}$ 180°, and $\{6,7\}$ 270°. Again, identifiers are then counted upwards, increasing first per tetromino type and then per rotation.

The scenarios used are created by filling the available space randomly with tetrominoes in a non-overlapping manner and flush alignment. For the scenarios considered here, the tetrominoes are chosen either from the entire set or only from a defined subset. Additionally, we fill the remaining empty space at the outer boundaries. This is done to avoid narrow spaces between the TETRIS geometry and the outer walls. As the geometry is intended to represent shelves, which are usually placed with the back side directly to the outer walls, this measure avoids situations which would be unrealistic in the supermarket scenario at hand and could distort measurements with respect to exposure times.

For evaluation purposes, we determine several quantities regarding the tetromino grid of the main area. Firstly, we calculate heatmaps $H_{\text{frame}} \in \mathbb{R}^{20\times 33}$ (same size as grid area) as the histogram of the agents' trajectory positions for each time-frame. A heatmap

can be interpreted as the sum of the duration of stay (in seconds) of all agents visiting a grid cell within the given interval. This way, we can determine the relation of aerosol concentration to general activity at a certain location. As the heatmap does not give explicit information about the number of agents visiting a grid cell, we additionally count the number of individuals and store it as $I_{\text{frame}} \in \mathbb{R}^{20\times 33}$. Finally, we calculate a map $D_{\text{frame}} \in \mathbb{R}^{20\times 33}$, storing the distance at each (walkable) position from the entrance area. This was done by using the fast-marching method [41] to determine the distance from the middle starting point (shown in green at the upper right in Figure 2), resulting in a (intermediate) map $\phi^{\text{dist}}_{\text{frame}} \in \mathbb{R}^{h_F\times w_F}$. From this map, we calculate $D_{\text{frame}} \in \mathbb{R}^{20\times 33}$ by calculating the (arithmetic) mean value within each grid cell from $\phi^{\text{dist}}_{\text{frame}}$.

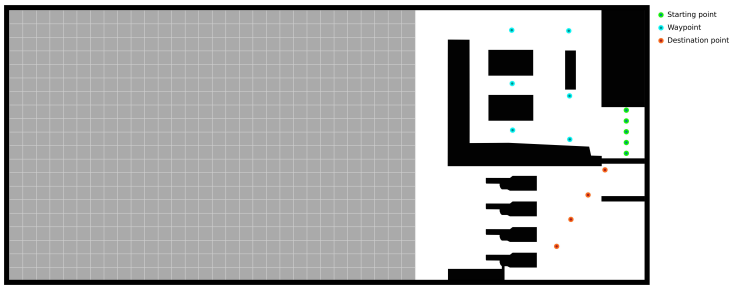

Figure 2. Basic floor plan with entry (upper right), cashier, and exit areas (lower right) with static points, and empty grid for Tetris geometry (left, shown in gray).

Tetromino subblocks are categorized into different types regarding the shape, or more precisely, the angle of the actual geometry at the subblock. This is done to quantify the influence of the geometry. We define the set of possible cases as $A = \{\text{convex, concave, edge, straight}\}$. If the subblock contains an inner corner, it is classified as concave, and if it is at the tip of an outer corner, it is classified as convex. Concave subblocks are, for example (cf. Figure 3), 005, 037, and 006, and convex ones are 031, 053, 077. A subblock is classified as an edge if it is located at the tip of a straight line, e.g., 009 or 010. All other subblocks are classified as straight, meaning they are located next to a straight wall. Examples include subblocks 022, 054, and 078.

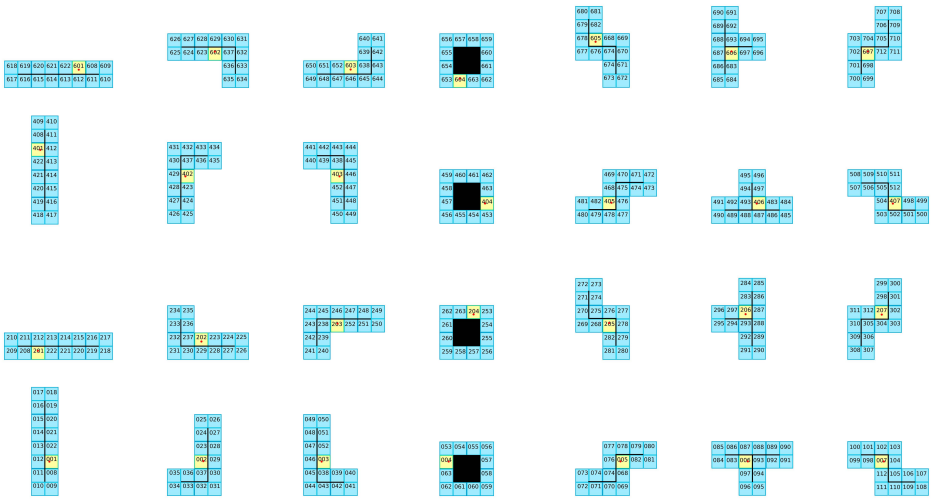

Figure 3. The whole set of tetrominoes used, with unique numbering of subblocks shown. Initial configuration is shown in the bottom row; other rows show rotated versions.

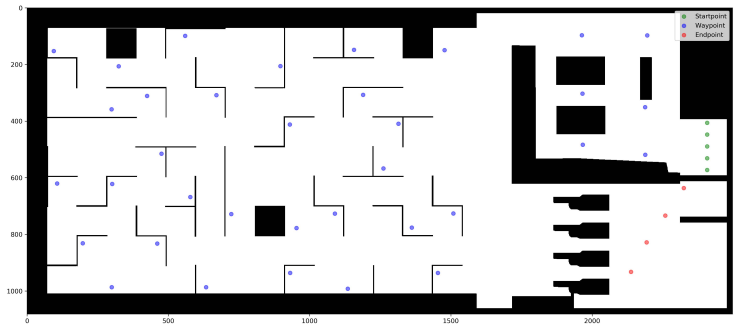

(**a**)

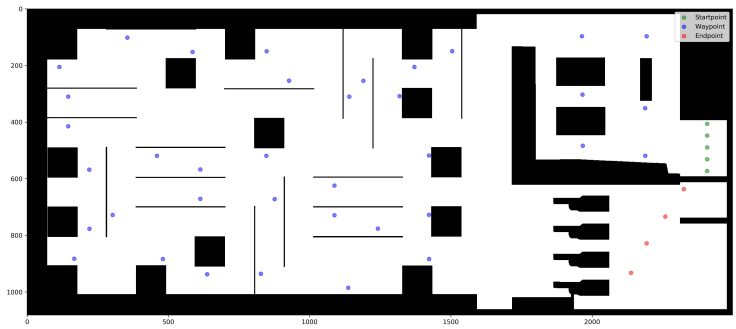

(**b**)

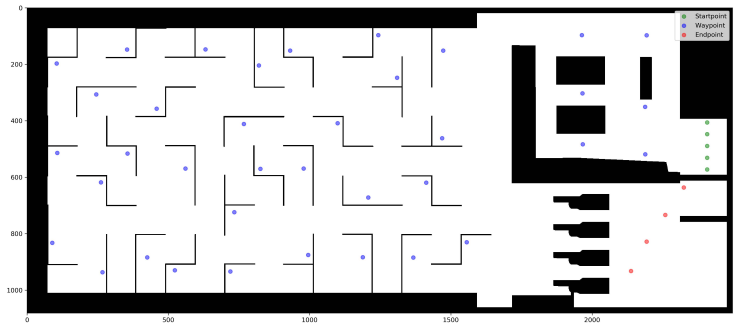

(**c**)

Figure 4. Illustration of randomly generated scenarios with different tetromino shapes: (**a**) Scenario 1 floor plan and POI (all tetrominoes used). (**b**) Scenario 2 floor plan and POI (I and O tetrominoes). (**c**) Scenario 3 (J, L, S, T, Z tetrominoes). Black areas indicate obstacles.

4. Experiments

We consider three distinct scenarios, in which we vary the TETRIS-based geometry in the main area of the floor plan and the composition of tetrominoes. The geometry is created in a random manner and the corresponding scenarios differ in terms of the tetromino shapes used.

In the first one (Figure 4a), the blocks are drawn from all seven available shapes. In the second scenario (Figure 4b), only I and O shapes are used, while in the third one, J, L, S, T, and Z blocks are used (Figure 4c). These classifications were made with respect to the assumed accessibility or reachability of the waypoints in the individual shapes. As shown in Figure 1, the waypoints of the I and O shapes are directly reachable from three directions, while the waypoints of the J and L shapes are partially obstructed from one direction due to the nearby right angle of the walls. In addition, the waypoints of shapes S, T, and Z are located directly in the corners, potentially forcing agents into even more complex trajectories to reach them. For all three variants, we additionally created "empty" equivalents, i.e., the TETRIS geometry was removed entirely from the main area, but the

waypoints implied by the tetrominoes were kept. This way, we seek to gain insight about the influence of the tetromino blocks on the exposure to viral load of the agents.

Based on these configurations, we ran simulations with the following parameters. Each simulation was run with a number of $n = 150$ agents at the same time and an agent pool of size $\left|P_{\text{pool}}\right| = 1000$. The duration of each run was set to $t_{\max} = 9500$ s. To get more meaningful figures, each configuration of the simulation was run ten times. The time frame for aerosol calculations was set to $t_{\text{frame}} = 500$ s; the values $c_i^{\text{ae}}(t)$ determining the viral load emitted by an infected agent is determined at each time t for each agent when calculating an aerosol map ϕ_j^{ae}. The corresponding radius is set to $r_{\text{ae}} = 0.5$ m [42]. The agents' desired speed v^0 was sampled from a normal distribution $\mathcal{N}\left(1.29, 0.19^2\right)$, representing average pedestrian walking speed [36]. The Boolean value c_i, determining infectiousness, was sampled from a Bernoulli distribution with probability 0.02, which equals a realistic incidence of 2% during the COVID-19 pandemic [15,43]. The viral load of tidal air was assumed as 5×10^8 RNA copies/cm^3 [44], and the respiration rate as 6^{-1} L/s, both together determining the deposited aerosol load per area and time. Figure 5 shows exemplary aerosol maps ϕ^{ae} for the individual scenarios.

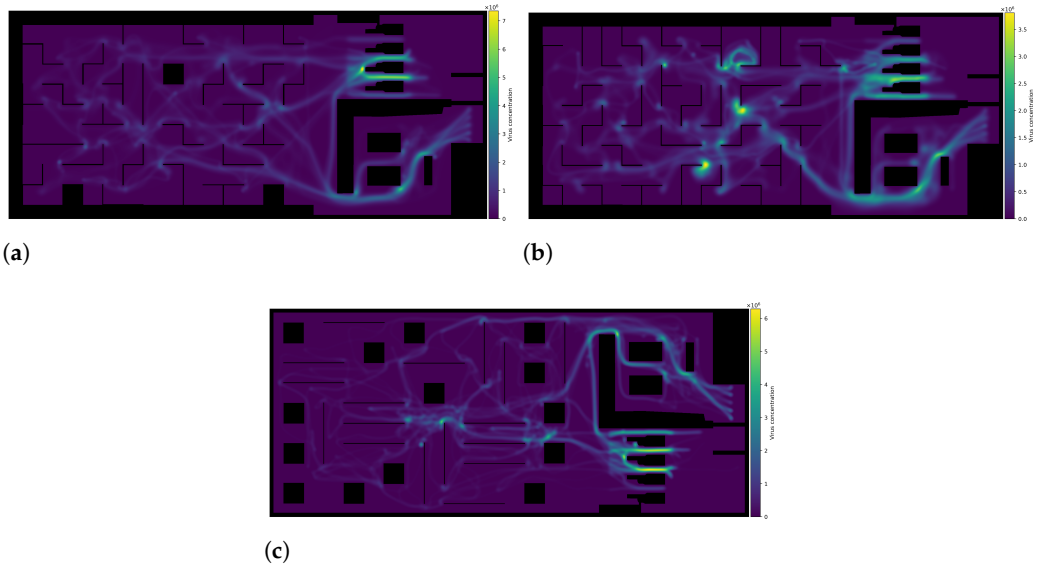

(**a**) (**b**)

(**c**)

Figure 5. Exemplary aerosol maps ϕ^{ae} for each scenario: (**a**) all tetrominoes; (**b**) JLSTZ; (**c**) IO. Black areas indicate obstacles.

We evaluate our simulation results with respect to agent movement and aerosol concentration based on the grid structure in the main area, as implied by the tetromino subblocks (see Figure 6). The evaluation can be divided into two main parts. On the one hand, we analyze the agent count and aerosol concentration descriptively over time. This is done based on the division into time frames, as mentioned earlier. On the other hand, we train an artificial neural network (ANN) in order to test if grid cells can be assigned to their location relative to tetromino geometry. More precisely, we analyze if grid cells can be reliably assigned to corner or flat positions.

We opted for using an ANN in addition to the descriptive analysis for two reasons. First, we wanted to analyze not only if differences between individual grid cells come about from different average/mean values, but if they can actually be distinguished based on the characteristics of the number of agents and aerosol concentrations over time. Secondly, we wanted to identify the input variables of particular relevance for the differentiation of tetrominoes with and without angular structures.

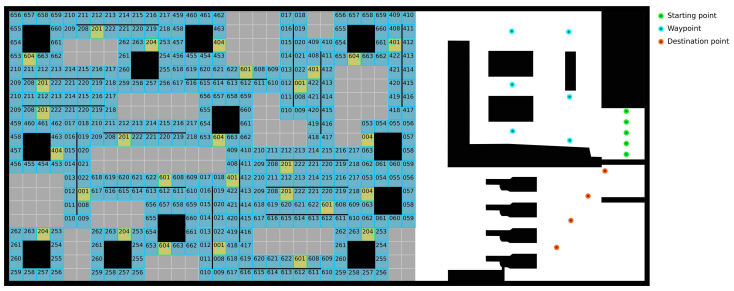

Figure 6. Example configuration with grid area filled with tetrominoes. Colors and numbers indicate block configuration, for more details refer to Section 3.5.

The ANN architecture used is an ensemble of 80 multilayer perceptrons, constituted of fully connected layers with a Rectified Linear Unit (ReLU) as the activation function [45]. Hyperparameter tuning was performed to determine suitable training parameters, such as the learning rate, dropout rate, and number of training epochs, with the final configuration selected based on validation performance [46]. The input layers consist of 60 variables, comprising the number of individual agents as well as the progress of heatmaps and aerosol concentration over time. The individual ANNs have three hidden layers with 10 neurons each and one output neuron predicting a corner or flat position. The networks were trained with the iRPROP+ algorithm [47] on 75% of the gathered samples. The results stem from the remaining 25%. To avoid biased performance estimates, the test set was strictly separated from the training data. We measure the classification rating by means of the accuracy (percentage of correct predictions) and the AUC value (area under the curve/area under the receiver operating characteristic).

5. Evaluation

We evaluated the three different scenarios ("All, IO, JLTSZ"), based on ten simulation runs each, with respect to the tetromino shapes used in all these simulations over time. In other words, we counted the number of visitations by the agents. This adds up to 1230 tetrominoes in total. The distribution (tetromino/count) with respect to the fundamental shapes is as follows: I: 430; O: 180; J: 90; L: 120; S: 190; T: 140; Z: 80.

Based on the data gathered from these scenarios, we analyze three configurations, where we juxtapose subsets of tetromino types with different properties. More precisely, we compare tetromino types differing in angularity and in the corresponding reachability of their waypoints. In this regard, tetrominoes I and O are entirely convex, and their waypoints are not obstructed, as shown in Figure 1. The other remaining tetrominoes all have inner corners with right-angle structures, making the waypoints harder to reach. Nevertheless, they can be still be differentiated further, depending on the placement of the waypoints with respect to the right angles. In this regard, the waypoints of L and J are supposedly easier to reach than the waypoints of S, T, and Z. We thus compare the convex tetrominoes I and O with the non-convex ones JLSTZ, which constitutes the first configuration IO_JLSTZ. In the second configuration, we move J and L to the first group, resulting in a comparison of I, O, J, and L, on the one hand, and S, T, and Z, on the other. This will be referred to as IOJL_STZ. In the last configuration, we only compare the convex tetrominoes I and O to the non-convex and hard-to-reach tetrominoes S, T, and Z. Accordingly, this configuration is called IO_STZ.

In the following, we analyze and compare these configurations quantitatively with respect to associated aerosol concentration. We also analyze how reliably these configurations can be predicted and classified by our ANN. This means that we analyze how well a grid position can be classified as a convex or non-convex tetromino subblock, based on the time-dependent aerosol concentration data from our simulation.

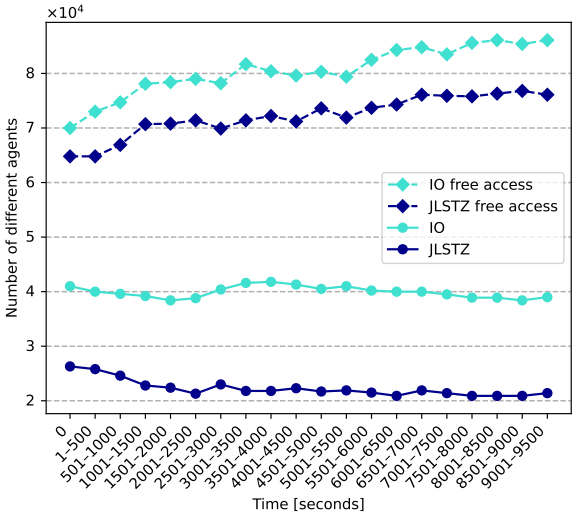

(**a**)

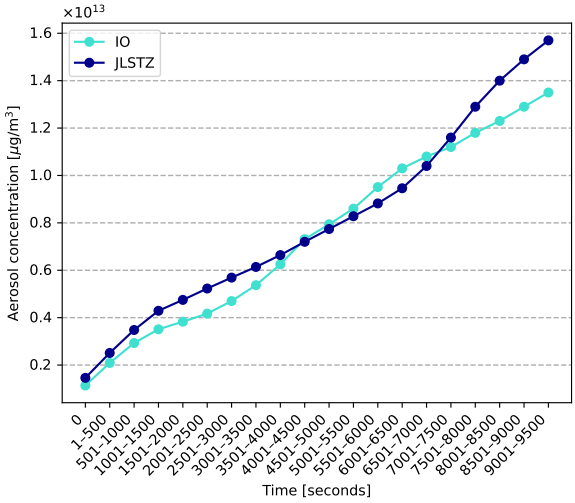

(**b**)

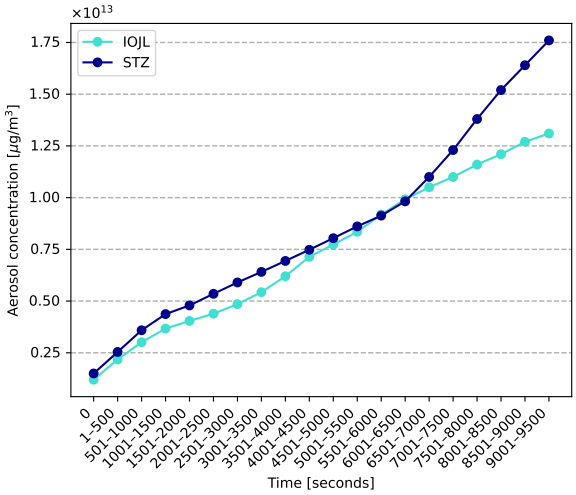

(**c**)

Figure 7. Time-related analyses. (**a**) Numbers of different agents over time (IO_JLSTZ). (**b**) Aerosol concentrations over time (IO_JLSTZ). (**c**) Aerosol concentrations over time (IOJL_STZ).

For the approach IO_JLSTZ, Figure 7a shows the number of individual agents over time. The solid lines show the averaged results for tetrominoes with and without angles; the dashed lines show the results for the hypothetical situation with the geometry removed, or, put differently, with the shelves not posing any hindrance to the agents. It can be seen that the number of agents is significantly lower for the tetrominoes with angular structures (JLSTZ). It can thus be assumed that congestions arise at the hotspots near the angular tetrominoes, which are harder to reach, thus impeding the influx of additional agents. This assumption is supported by the fact that the difficulty of reaching the waypoints gets more severe during the first time intervals, which can be seen from the decreasing number of individual agents at the hotspots of the angular tetrominoes. In order to rule out the possibility that the lower numbers of agents at the angular tetrominoes stem from those structures being supposedly harder to reach, for instance due to their placement within the floor plan, we also conducted the simulations with the tetromino geometry removed, as already described in Section 4. Exemplary agent trajectories are shown in Figure 8. From the resulting numbers (Figure 7a), it can be seen that this is not the case, as the numbers are still notably higher than the corresponding ones with the geometry still in place. Angular structures may appear to accumulate more aerosols; however, this may reflect limited accessibility for airflow, sampling, and cleaning rather than higher intrinsic deposition [48]. First and foremost, these numbers are within the same range as the numbers of the convex tetrominoes. Furthermore, Figure 7b shows the aerosol concentrations over time. While the value increases generally linearly for the tetrominoes without angular structure, it increases almost exponentially for the other tetrominoes from $t \approx 3500$ s. Additionally, a considerably higher concentration can be seen for the angular-structured tetrominoes at the end of the measurement period. The differences are even more pronounced in the IOJL_STZ approach (see Figure 7c).

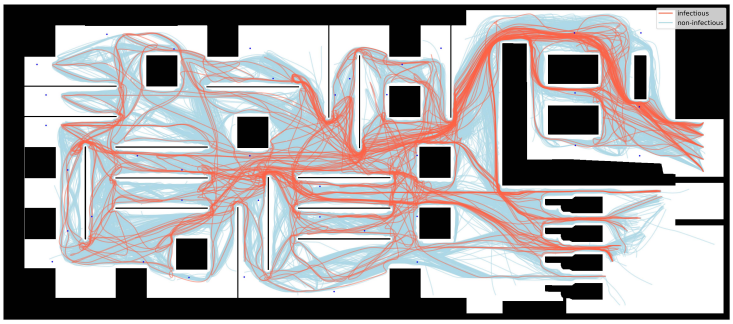

(**a**)

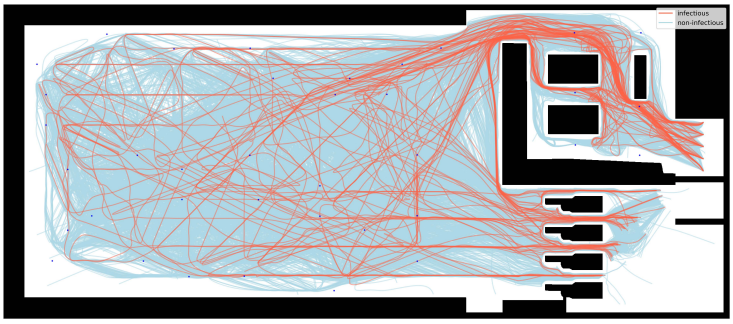

(**b**)

Figure 8. Exemplary agent trajectories: (**a**) trajectories scenario IO and (**b**) Trajectories scenario IO, empty equivalent. Black areas signify obstacles.

For all three approaches, the ANNs achieve very high classification rates, as shown in Table 2. This means that the characteristics of the compared tetromino types are significantly different. Thus, an obvious association between the shape of the tetromino and aerosol concentration exists. The AUC values also support previous findings that angular-structured tetrominoes exhibit different characteristics. The results of the sensitivity analysis show that the number of individual agents poses a significant input variable. In the approach IO_JLSTZ, this applies especially for the interval between 1001 s and 3500 s, while for the approach IOJL_STZ, this interval lies between 1001 s and 2000 s. The cause of this difference might stem from the fact that the congestion starts earlier for destinations which are harder to reach.

Table 2. ANN classification accuracy.

Configuration	Classification Rate	AUC
IO_JLSTZ	94%	0.98
IOJL_STZ	83%	0.91
IO_STZ	90%	0.98

6. Discussion

The present study was designed to determine whether constituents of this game, tetrominos, can be used to examine the frequency and duration of infection-risking behavior of individuals, agents, in the context of geometry and airborne respiratory pathogens (e.g., SARS-CoV-2).

Despite the fact that agent-based models are suited to capturing heterogeneity and individual behavioral changes [19], the trajectories found in the present study were, however, suggestive of a predominantly counter-clockwise direction of agent movement around the shop's perimeter, despite the fact that the agents themselves had no laterality bias [49]. This finding is in keeping with what has been described for stores with the entry situated on the right side of the shopping area [50]. The architectural design of a store is one of the keys to keeping customers busy with browsing and shopping for longer durations [51]. It has been reported that outlets with an interior architecture leading customers chiefly counter-clockwise tend to make shoppers walk longer distances to accomplish their shopping mission than stores with a more clockwise layout [52] (clockwise movement even facilitates arithmetic calculation in terms of addition in a subset of customers [53], which might at the end of the day reduce the quantity of purchases). As there is currently no direct, well-established link in the literature between the direction of movement within a shop (clockwise vs. anti-clockwise) and aerosol concentration, this could be investigated in more detail in future. The situation introduced here was therefore set up to generate trajectories resulting from a predominantly counter-clockwise direction of movement to reflect a retailer's desire to keep shoppers inside the store longer. This could, however, help increase the risk of infection. A couple of publications therefore discuss how in response to COVID-19, the trajectories of people may be revised inside buildings in an attempt to optimize the use of furniture such as shelves and temporary partitions as barriers [54,55].

The findings of the present study may be interpreted in light of the fact supermarkets tend to routinely locate popular items in the center of the aisles and as far from the entrance as possible to ensure that even the potentially most single-minded buyer will pass a plethora of tempting products. Mid-aisle positioning may be held accountable for the hotspots found in the simulation. It may be locus of debate whether hotspots should be considered rather irrelevant as air vortices produced by air conditioning and radiators as well as people moving around in for instance a supermarket can make a location far away from the source of the virus more dangerous than a location just two meters away [56]. In this context,

the simulation presented here could be vastly improved by incorporating methods from computational fluid dynamics (CFD) into the aerosol model [57,58].

7. Conclusions

In the present study, we have simulated and analyzed airborne infectious disease spread with an agent-based pedestrian model and a defined set of geometry, derived from the game TETRIS. The study shows that tetrominoes with angular structure significantly differ in terms of the characteristics of aerosol concentration over time, compared to tetrominoes lacking this angular structure. More precisely, the area on the inner or convex side of the angular structure shows the increased concentration of aerosol contamination. This association of location and concentration, which in part exhibits exponential rise, could be shown with the help of ANN.

For practical use, it can be deduced that supermarkets should preferably avoid angular structures and shelves, and especially structures with hard-to-reach corners (cf. tetrominoes S, T, and Z). Other possible mitigation strategies include increasing the width of aisles or considerate placement of points-of-interest. While this effect might not be pronounced with only few customers attending the store, in our simulation, with rising numbers it reaches figures relevant for infectious with airborne respiratory pathogens.

Author Contributions: Conceptualization, M.W. and T.H.; methodology, M.W., T.H., R.L. and F.W.; software, T.H. and R.L.; validation, T.H. and R.L.; formal analysis, T.H. and R.L.; investigation, M.W., T.H., R.L. and F.W.; resources, M.W., T.H. and F.W.; data curation, M.W., T.H. and R.L.; writing—original draft preparation, M.W., T.H., R.L.; writing—review and editing, F.W.; visualization, T.H. and R.L.; supervision, M.W. and F.W.; project administration, M.W. and F.W.; funding acquisition, F.W.; All authors have read and agreed to the published version of the manuscript.

Funding: This research received no external funding.

Data Availability Statement: The data presented in this study are available on request from the corresponding author due to privacy reasons.

Conflicts of Interest: The author declares no conflicts of interest.

References

1. Zhou, P.; Yang, X.; Wang, X.G.; Hu, B.; Zhang, L.; Zhang, W.; Si, H.R.; Zhu, Y.; Li, B.; Huang, C.L.; et al. A pneumonia outbreak associated with a new coronavirus of probable bat origin. *Nature* **2020**, *579*, 270–273. [CrossRef]
2. World Health Organization. *Coronavirus Disease (COVID-2019) Situation Report 147 (15 June 2020)*; World Health Organization: Geneva, Switzerland, 2020.
3. Dong, E.; Du, H.; Gardner, L. An interactive web-based dashboard to track COVID-19 in real time. *Lancet Infect Dis.* **2020**, *20*, 533–534. [CrossRef]
4. Mackie, P. The classification of viruses infecting the respiratory tract. *Paediatr. Respir. Rev.* **2003**, *4*, 84–90. [CrossRef]
5. Gavane, V. Human Respiratory Viruses: Mechanisms, Epidemiology, Morbidity, and Contemporary Challenges to Global Health. *Biopress J. Adv. Pharmacol. (BJAP)* **2025**, *1*, 28–34.
6. Yassin, M.; Almouqatea, S. Assessment of airborne bacteria and fungi in an indoor and outdoor environment. *Int. J. Environ. Sci. Technol.* **2010**, *7*, 535–544. [CrossRef]
7. Leung, N.H.L. Transmissibility and transmission of respiratory viruses. *Nat. Rev. Microbiol.* **2021**, *19*, 528–545. [CrossRef] [PubMed]
8. Martin-Neuninger, R.; Ruby, M.B. What Does Food Retail Research Tell Us About the Implications of Coronavirus (COVID-19) for Grocery Purchasing Habits? *Front. Psychol.* **2020**, *11*, 1448. [CrossRef]
9. Vuorinen, V.; Aarnio, M.; Alava, M.; Alopaeus, V.; Atanasova, N.; Auvinen, M.; Balasubramanian, N.; Bordbar, H.; Erästö, P.; Grande, R.; et al. Modelling aerosol transport and virus exposure with numerical simulations in relation to SARS-CoV-2 transmission by inhalation indoors. *Saf. Sci.* **2020**, *130*, 104866. [CrossRef]
10. Tsukanov, A.A.; Senjkevich, A.M.; Fedorov, M.V.; Brilliantov, N.V. How risky is it to visit a supermarket during the pandemic? *PLoS ONE* **2021**, *16*, e0253835. [CrossRef]

11. Segal-Halevi, E.; Nitzan, S.; Hassidim, A.; Aumann, Y. Fair and square: Cake-cutting in two dimensions. *J. Math. Econ.* **2017**, *70*, 1–28. [CrossRef]
12. Gao, P.; Gu, A.; Zakhor, A. Optical proximity correction with principal component regression. In *Proceedings of the Optical Microlithography XXI*; Levinson, H.J., Dusa, M.V., Eds.; International Society for Optics and Photonics, SPIE: Bellingham, WA, USA, 2008, Volume 6924, p. 69243N. [CrossRef]
13. Korn, M.; Pak, I. Tilings of rectangles with T-tetrominoes. *Theor. Comput. Sci.* **2004**, *319*, 3–27. [CrossRef]
14. Pérez-Latorre, Ó. From Chess to StarCraft. A Comparative Analysis of Traditional Games and Videogames. *Comunicar* **2012**, *19*, 121–129. [CrossRef]
15. Harweg, T.; Bachmann, D.; Weichert, F. Agent-based simulation of pedestrian dynamics for exposure time estimation in epidemic risk assessment. *J. Public Health* **2021**, *31*, 221–228. [CrossRef]
16. Adiga, A.; Dubhashi, D.; Lewis, B.; Marathe, M.; Venkatramanan, S.; Vullikanti, A. Mathematical Models for COVID-19 Pandemic: A Comparative Analysis. *J. Indian Inst. Sci.* **2020**, *100*, 793–807. [CrossRef] [PubMed]
17. Shao, S.; Zhou, D.; He, R.; Li, J.; Zou, S.; Mallery, K.; Kumar, S.; Yang, S.; Hong, J. Risk assessment of airborne transmission of COVID-19 by asymptomatic individuals under different practical settings. *J. Aerosol Sci.* **2021**, *151*, 105661. [CrossRef] [PubMed]
18. Vespignani, A.; Tian, H.; Dye, C.; Lloyd-Smith, J.O.; Eggo, R.M.; Shrestha, M.; Scarpino, S.V.; Gutierrez, B.; Kraemer, M.U.G.; Wu, J.; et al. Modelling COVID-19. *Nat. Rev. Phys.* **2020**, *2*, 279–281. [CrossRef]
19. Agrawal, S.; Bhandari, S.; Bhattacharjee, A.; Deo, A.; Dixit, N.M.; Harsha, P.; Juneja, S.; Kesarwani, P.; Swamy, A.K.; Patil, P.; et al. City-Scale Agent-Based Simulators for the Study of Non-pharmaceutical Interventions in the Context of the COVID-19 Epidemic. *J. Indian Inst. Sci.* **2020**, *100*, 809–847. [CrossRef]
20. Mahmood, I.; Arabnejad, H.; Suleimenova, D.; Sassoon, I.; Marshan, A.; Serrano-Rico, A.; Louvieris, P.; Anagnostou, A.; Taylor, S.J.E.; Bell, D.; et al. FACS: A geospatial agent-based simulator for analysing COVID-19 spread and public health measures on local regions. *J. Simul.* **2020**, *16*, 355–373. [CrossRef]
21. Madewell, Z.J.; Yang, Y.; Longini, I.M.; Halloran, M.E.; Dean, N.E. Household Transmission of SARS-CoV-2. *JAMA Netw. Open* **2020**, *3*, e2031756. [CrossRef]
22. Cuevas, E. An agent-based model to evaluate the COVID-19 transmission risks in facilities. *Comput. Biol. Med.* **2020**, *121*, 103827. [CrossRef] [PubMed]
23. Shamil, M.S.; Farheen, F.; Ibtehaz, N.; Khan, I.M.; Rahman, M.S. An Agent-Based Modeling of COVID-19: Validation, Analysis, and Recommendations. *Cogn. Comput.* **2021**, *16*, 1723–1734. [CrossRef] [PubMed]
24. Chong, M.Y.; An, H.; Wang, P.C.; Soh, C.B.; Chien, S.C.; Roch, E.R.; Koh, J.J.; Yu, S.C.M. Multiscale modelling and infection probability of SARS-CoV-2 transmission in a typical lecture theatre. *Build. Environ.* **2025**, *269*, 112407. [CrossRef]
25. Shah, S.M.A.; Nie, Y.; Din, A.; Alkhazza, A.; Arshad, A.; Younas, B. Stochastic modeling for the transmission of hepatitis B virus with multiple time-delays and vaccination effect. *Arab. J. Math.* **2025**, *14*, 525–554. [CrossRef]
26. Papathanasopoulou, V.; Perakis, H.; Spyropoulou, I.; Gikas, V. Pedestrian simulation challenges: Modeling techniques and emerging positioning technologies for its applications. *IEEE Trans. Intell. Transp. Syst.* **2024**, *25*, 12876–12892. [CrossRef]
27. Caramuta, C.; Collodel, G.; Giacomini, C.; Gruden, C.; Longo, G.; Piccolotto, P. Survey of detection techniques, mathematical models and simulation software in pedestrian dynamics. *Transp. Res. Procedia* **2017**, *25*, 551–567. [CrossRef]
28. Williams, K.; Ostwald, M.J. Manifestations of Geometry in Architecture. *Nexus Netw. J.* **2017**, *19*, 1–3. [CrossRef]
29. Breukelaar, R.; Demaine, E.D.; Hohenberger, S.; Hoogeboom, H.J.; Kosters, W.A.; Liben-Nowell, D. Tetris is Hard, Even to Approximate. *Int. J. Comput. Geom. Appl.* **2004**, *14*, 41–68. [CrossRef]
30. Burgiel, H. How to lose at Tetris. *Math. Gaz.* **1997**, *81*, 194–200. [CrossRef]
31. Merino, C. On the number of tilings of the rectangular board with T-tetronimoes. *Australas. J. Comb.* **2008**, *41*, 107–114.
32. Haier, R.J.; Karama, S.; Leyba, L.; Jung, R.E. MRI assessment of cortical thickness and functional activity changes in adolescent girls following three months of practice on a visual-spatial task. *BMC Res. Notes* **2009**, *2*, 174. [CrossRef]
33. Lau-Zhu, A.; Holmes, E.A.; Butterfield, S.; Holmes, J. Selective Association Between Tetris Game Play and Visuospatial Working Memory: A Preliminary Investigation. *Appl. Cogn. Psychol.* **2017**, *31*, 438–445. [CrossRef]
34. Le, A.; Arunmozhi, M.; Veerajagadheswar, P.; Ku, P.C.; Minh, T.H.; Sivanantham, V.; Mohan, R. Complete Path Planning for a Tetris-Inspired Self-Reconfigurable Robot by the Genetic Algorithm of the Traveling Salesman Problem. *Electronics* **2018**, *7*, 344. [CrossRef]
35. Majerowitz, M.; Allweil, Y. Housing in the Neoliberal City: Large Urban Developments and the Role of Architecture. *Urban Plan.* **2019**, *4*, 43–61. [CrossRef]
36. Moussaïd, M.; Helbing, D.; Garnier, S.; Johansson, A.; Combe, M.; Theraulaz, G. Experimental study of the behavioural mechanisms underlying self-organization in human crowds. *Proc. R. Soc. B Biol. Sci.* **2009**, *276*, 2755–2762. [CrossRef] [PubMed]
37. Borgefors, G. Distance transformations in digital images. *Comput. Vis. Graph. Image Process.* **1986**, *34*, 344–371. [CrossRef]
38. Felzenszwalb, P.F.; Huttenlocher, D.P. Distance transforms of sampled functions. *Theory Comput.* **2012**, *8*, 415–428. [CrossRef]
39. Dijkstra, E.W. A note on two problems in connexion with graphs. *Numer. Math.* **1959**, *1*, 269–271. [CrossRef]

40. Dong, J.; Li, L.; Huang, J.; Han, D. ISOVIST BASED ANALYSIS OF SUPERMARKET LAYOUT—Verification of Visibility Graph Analysis and Multi-Agent Simulation. In Proceedings of the 11th International Space Syntax Symposium, Lisbon, Portugal, 3–7 July 2017.
41. Sethian, J.A. A fast marching level set method for monotonically advancing fronts. *Proc. Natl. Acad. Sci. USA* **1996**, *93*, 1591–1595. [CrossRef]
42. Chen, W.; Zhang, N.; Wei, J.; Yen, H.L.; Li, Y. Short-range airborne route dominates exposure of respiratory infection during close contact. *Build. Environ.* **2020**, *176*, 106859. [CrossRef]
43. Wang, T.; Li, C.; Li, H.; Li, Z. Urban monitoring, evaluation and application of COVID-19 listed vaccine effectiveness: A health code blockchain study. *BMJ Open* **2022**, *12*, e057281. [CrossRef]
44. Lelieveld, J.; Helleis, F.; Borrmann, S.; Cheng, Y.; Drewnick, F.; Haug, G.; Klimach, T.; Sciare, J.; Su, H.; Pöschl, U. Model Calculations of Aerosol Transmission and Infection Risk of COVID-19 in Indoor Environments. *Int. J. Environ. Res. Public Health* **2020**, *17*, 8114. [CrossRef] [PubMed]
45. Foukalas, F. A survey of artificial neural network computing systems. *Cogn. Comput.* **2025**, *17*, 4. [CrossRef]
46. Bartz-Beielstein, T. Hyperparameter Tuning. In *Online Machine Learning: Eine Praxisorientierte Einführung*; Springer: Wiesbaden, Germany, 2024; pp. 123–150.
47. Igel, C.; Hüsken, M. Empirical evaluation of the improved Rprop learning algorithms. *Neurocomputing* **2003**, *50*, 105–123. [CrossRef]
48. Nazaroff, W.W. Indoor particle dynamics. *Indoor Air* **2004**, *14*, 175–183. [CrossRef]
49. Karim, A.K.M.R.; Proulx, M.J.; de Sousa, A.A.; Karmaker, C.; Rahman, A.; Karim, F.; Nigar, N. The right way to kiss: Directionality bias in head-turning during kissing. *Sci. Rep.* **2017**, *7*, 5398. [CrossRef]
50. Sorensen, H. The Science of Shopping. *Mark. Res.* **2003**, *15*, 30–35.
51. Gogoi, B.J. Effect of Store Design on Perceived Crowding and Impulse Buying Behavior. *Int. Rev. Manag. Mark.* **2017**, *7*, 180–186.
52. Groeppel-Klein, A.; Bartmann, B. Anti-Clockwise or Clockwise? The Impact of Store Layout on the Process of Orientation in a Discount Store. In *Proceedings of the Association for Consumer Research*; Borghini, S., McGrath, M.A., Otnes, C., Eds.; Association for Consumer Research: Duluth, MN, USA, 2007; Volume 8, pp. 415–416.
53. Lugli, L.; D'Ascenzo, S.; Borghi, A.M.; Nicoletti, R. Clock Walking and Gender: How Circular Movements Influence Arithmetic Calculations. *Front. Psychol.* **2018**, *9*, 1599. [CrossRef]
54. Antonenko, N.; Rumilets, T. COVID-19 and Library Public Space Transformations. *Archit. Civ. Eng. Environ.* **2020**, *13*, 5–18. [CrossRef]
55. Romero, V.; Stone, W.D.; Ford, J.D. COVID-19 indoor exposure levels: An analysis of foot traffic scenarios within an academic building. *Transp. Res. Interdiscip. Perspect.* **2020**, *7*, 100185. [CrossRef]
56. Anchordoqui, L.A.; Chudnovsky, E.M. A Physicist View of COVID-19 Airborne Infection through Convective Airflow in Indoor Spaces. *SciMedicine J.* **2020**, *2*, 68–72. [CrossRef]
57. Ren, C.; Xi, C.; Wang, J.; Feng, Z.; Nasiri, F.; Cao, S.J.; Haghighat, F. Mitigating COVID-19 infection disease transmission in indoor environment using physical barriers. *Sustain. Cities Soc.* **2021**, *74*, 103175. [CrossRef] [PubMed]
58. Sarhan, A.R.; Naser, P.; Naser, J. COVID-19 aerodynamic evaluation of social distancing in indoor environments, a numerical study. *J. Environ. Health Sci. Eng.* **2021**, *19*, 1969–1978. [CrossRef] [PubMed]